Bio-Design and Manufacturing (2024) 7:74–87
https://doi.org/10.1007/s42242-023-00259-x

RESEARCH ARTICLE

Customized scaffolds for large bone defects using 3D-printed modular blocks from 2D-medical images

Anil A. Acar[1,2] · Evangelos Daskalakis[3] · Paulo Bartolo[3,4] · Andrew Weightman[3] · Glen Cooper[3] · Gordon Blunn[5] · Bahattin Koc[1,2]

Received: 2 February 2023 / Accepted: 14 September 2023 / Published online: 15 December 2023

Abstract

Additive manufacturing (AM) has revolutionized the design and manufacturing of patient-specific, three-dimensional (3D), complex porous structures known as scaffolds for tissue engineering applications. The use of advanced image acquisition techniques, image processing, and computer-aided design methods has enabled the precise design and additive manufacturing of anatomically correct and patient-specific implants and scaffolds. However, these sophisticated techniques can be time-consuming, labor-intensive, and expensive. Moreover, the necessary imaging and manufacturing equipment may not be readily available when urgent treatment is needed for trauma patients. In this study, a novel design and AM methods are proposed for the development of modular and customizable scaffold blocks that can be adapted to fit the bone defect area of a patient. These modular scaffold blocks can be combined to quickly form any patient-specific scaffold directly from two-dimensional (2D) medical images when the surgeon lacks access to a 3D printer or cannot wait for lengthy 3D imaging, modeling, and 3D printing during surgery. The proposed method begins with developing a bone surface-modeling algorithm that reconstructs a model of the patient's bone from 2D medical image measurements without the need for expensive 3D medical imaging or segmentation. This algorithm can generate both patient-specific and average bone models. Additionally, a biomimetic continuous path planning method is developed for the additive manufacturing of scaffolds, allowing porous scaffold blocks with the desired biomechanical properties to be manufactured directly from 2D data or images. The algorithms are implemented, and the designed scaffold blocks are 3D printed using an extrusion-based AM process. Guidelines and instructions are also provided to assist surgeons in assembling scaffold blocks for the self-repair of patient-specific large bone defects.

Graphic abstract

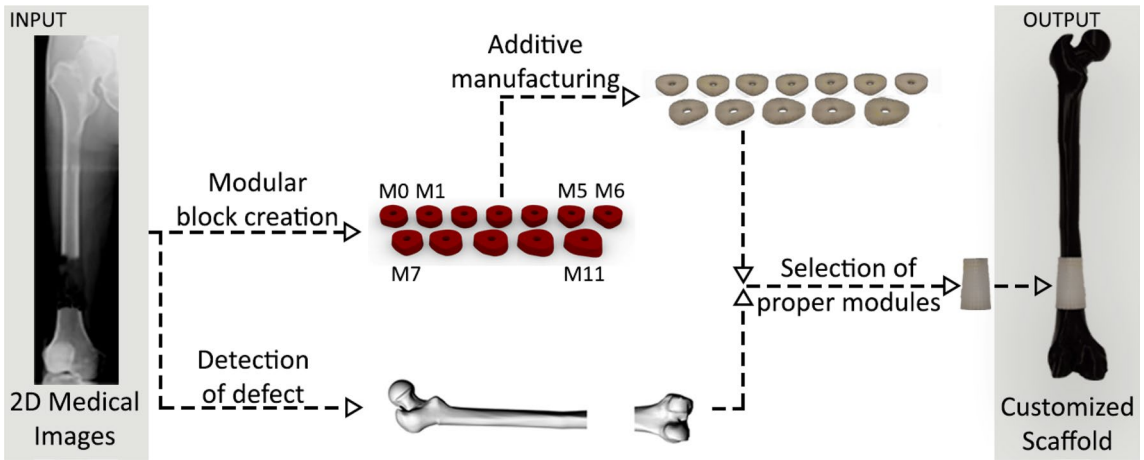

Keywords Additive manufacturing · Modular scaffolds · Large bone defect · Customized scaffold design · Patient-specific scaffolds

Extended author information available on the last page of the article

Introduction

Bone has a unique healing potential for self-regeneration after damage, especially for minor defects. However, external intervention is required for the self-repair of large defects that are greater than twice the diameter of the long bone diaphysis [1]. Autografts and allografts are external interventions that can aid bone regeneration. Nonetheless, the source of autografts is limited for filling of large bone defects or fractures. Additionally, extracting the autograft needs an additional surgical procedure that causes several problems [2–5]. Although allografts can be implemented in larger quantities, accessing the resources is not always easy, especially when the treatment is urgently needed, and the immune system of the patient can also reject the allografts.

In recent years, porous scaffolds have been used for healing bone defects and for bone regeneration. Bone scaffolds can be manufactured with different materials that must be biocompatible, bioresorbable, osteoconductive, and osteoinductive, and contain other cost-effective features (e.g., metals, ceramics, and polymers) [6]. Additionally, bone scaffolds should have a porous inner structure that provides a suitable environment for cells to maintain cell activity. These scaffold structures can be manufactured with several traditional methods such as gas foaming [7], freeze-drying [8], fiber sintering [9], and electrospinning [10]. However, these methods lack controllable pore characteristics, such as pore size, pore shape, and porosity, and this can negatively affect cellular distribution and nutrient and metabolite exchange, and thus cellular activity. This uncontrollable structure can cause nonuniform stress distribution inside the scaffold to create unpredicted mechanical properties. Furthermore, these methods may leave toxic residues inside the scaffold that will adversely affect the bone regeneration [11]. However, with additive manufacturing (AM) technology, bone scaffolds can be precisely manufactured with the desired interconnected porous inner structure that provides the necessary biological and mechanical properties with an appropriate external shape.

Designing a scaffold that meets the requirements of all patients is challenging, considering the differences in anatomy and morphology among people of different races, genders, and ages [12–15]. Furthermore, each bone shape and defect size is unique, and if a scaffold does not match the area accurately, a surgeon may have to modify the scaffold during the operation. This can increase the duration of the surgery and the risk of complications such as prolonged hospitalization, severe pain, and limb loss [14]. These complications can be avoided if scaffolds are custom designed and based on the unique anatomical and morphological features of the specific patient.

By importing two-dimensional (2D) medical imaging scans such as computed tomography (CT) or magnetic resonance imaging into medical image processing software, a three-dimensional (3D) model representing the fracture or bone defect area of a patient can be generated [16]. With computer-aided design systems, a virtual prototype of a customized bone substitute can be designed based on the obtained defect area model [17]. Technical and surgical staff then collaborate to ensure that the final design meets the unique anatomic features of the patient. With computer-aided manufacturing systems and AM, a more precise patient-specific scaffold that fits the unique anatomic features of the patient and the injury can be produced.

The use of AM to produce personalized scaffolds for bone regeneration is a promising solution but is also time-consuming, labor-intensive, and expensive [18]. Designing and manufacturing a single implant can take months, making this unsuitable for trauma patients or urgent cases. The process also requires access to expensive equipment for clinical imaging and medical image processing that may not be readily available in underdeveloped or resource-limited areas [19]. Thus, while AM of personalized scaffolds is a promising solution, its limitations in terms of cost and accessibility need to be considered.

In this study, we introduce the concept of creating a customized best-fitting scaffold from a range of readily manufactured, Lego-like "modules." The goal is to produce enough variety in modules with a rational product family architecture to enable provision of an improved patient-specific solution. Computational geometry-based algorithms were generated to model the bone surface and create the palette of modular blocks directly from 2D medical images or measurements. To manufacture the blocks with the desired properties, a parametric algorithm providing a deposition path planning for continuous extrusion AM was generated. A final algorithm was developed to guide the clinician on selecting and assembling the appropriate modules from the palette.

Methodology

The overall procedure for the developed method is shown in Fig. 1. The creation of patient-specific scaffold structure from 2D medical images is performed by Algorithm IV, which uses two further algorithms: a bone surface modeling algorithm and a modular block creation algorithm. The bone surface modeling algorithm generates a patient-specific 3D bone model from 2D medical images or average anthropometric measurements of a particular group (age, pathology, and gender), whereas the modular block creation algorithm generates modular scaffold blocks from the patient-specific or average bone model. The femur model and its parameters

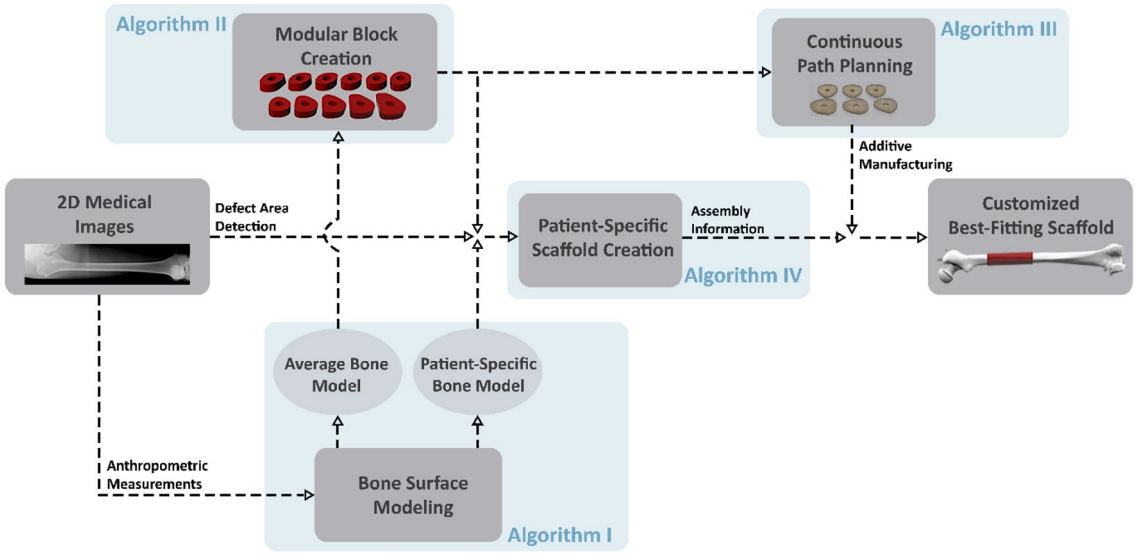

Fig. 1 Schematic diagram of the created method for generating a best-fitting scaffold directly from 2D medical images

can change based on anthropometric, age, pathological, and gender differences, and must be specified per group. Algorithm IV stores the morphological information of the modular scaffold blocks and the patient-specific bone model, and using the measurements extracted from 2D medical images, creates a customized scaffold structure with modular blocks. The algorithm provides assembly information to the surgeon about how many and which modular blocks to use to match the bone defect of the patient. The surgeon then selects the correct scaffold blocks from a palette of modules, containing already printed porous biodegradable structures, and assembles them as instructed by the algorithm to create the best-fitting scaffold for the patient.

3D parametric modeling of femur

Algorithm I (Fig. 1) can be used to model different bone surfaces. Here, we used the femur as an example. The femur has unique anatomical and morphological features, so parameterizing it is crucial to creating the best-fitting scaffold. This is achieved by defining referential geometrical entities (RGEs), which represent the unique morphological surface features of the femur and are important for orthopedic and trauma specialists. These RGEs, such as characteristic points, views, planes, and directions, are created based on the anatomic and mechanical axes and are referred to as the defined RGEs. These RGEs are shown in Fig. 2a and described in Table 1 [20–22]. Like planes and directions, every element used to remodel the femur geometry (i.e., anatomic and mechanical axes) is also defined as an RGE.

To acquire the external surface of the femur, a reverse engineering technique was performed. The obtained femur model was imported into the developed algorithm based on published studies [23, 24]. In this algorithm, the specified RGEs are extracted from the femur model. Using the designated RGEs, the anatomical coordinate system of the femur is constructed according to the International Society of Biomechanics suggestions [25]. While constructing the coordinate system, specific conditions are met: (1) the anatomical axis of the femur is vertical; (2) the epicondylar axis is parallel to the coronal plane [26]. It is assumed that this will be the case for any future femur models.

The defined RGEs are used when the femur model is divided into five regions. These regions are the head, neck, trochanter (greater and lesser), shaft, and condyle (Fig. 2c). These regions are used to perform local changes on the femur model, so a new femur model of a patient or a specific group could be obtained. Using the RGEs, the necessary auxiliary planes (e.g., Pl_{NT} and Pl_{TS}) are defined between these regions. Moreover, boundary curves between neighboring regions (e.g., head–neck and shaft–condyle) are created. Within these boundary curves, the femur model is sliced with multiplanes, and cross-sectional curves of those five regions are created. For these curves to be compatible with the femur to be generated, a new set of correct and necessary feature parameters (FPs) is introduced in every defined region (Table 2). The defined femoral feature morphologies (e.g., r_{FH}, L_N) have direct effects on femoral biomechanical functions [15]. Moreover, they can be easily extracted from 2D medical images (e.g., X-rays of the femur taken at coronal and sagittal planes) (Figs. 2a and 2b). The defined FPs are sufficient to make local morphological changes on the femur model within those regions, but they do not support making necessary arrangements to the whole

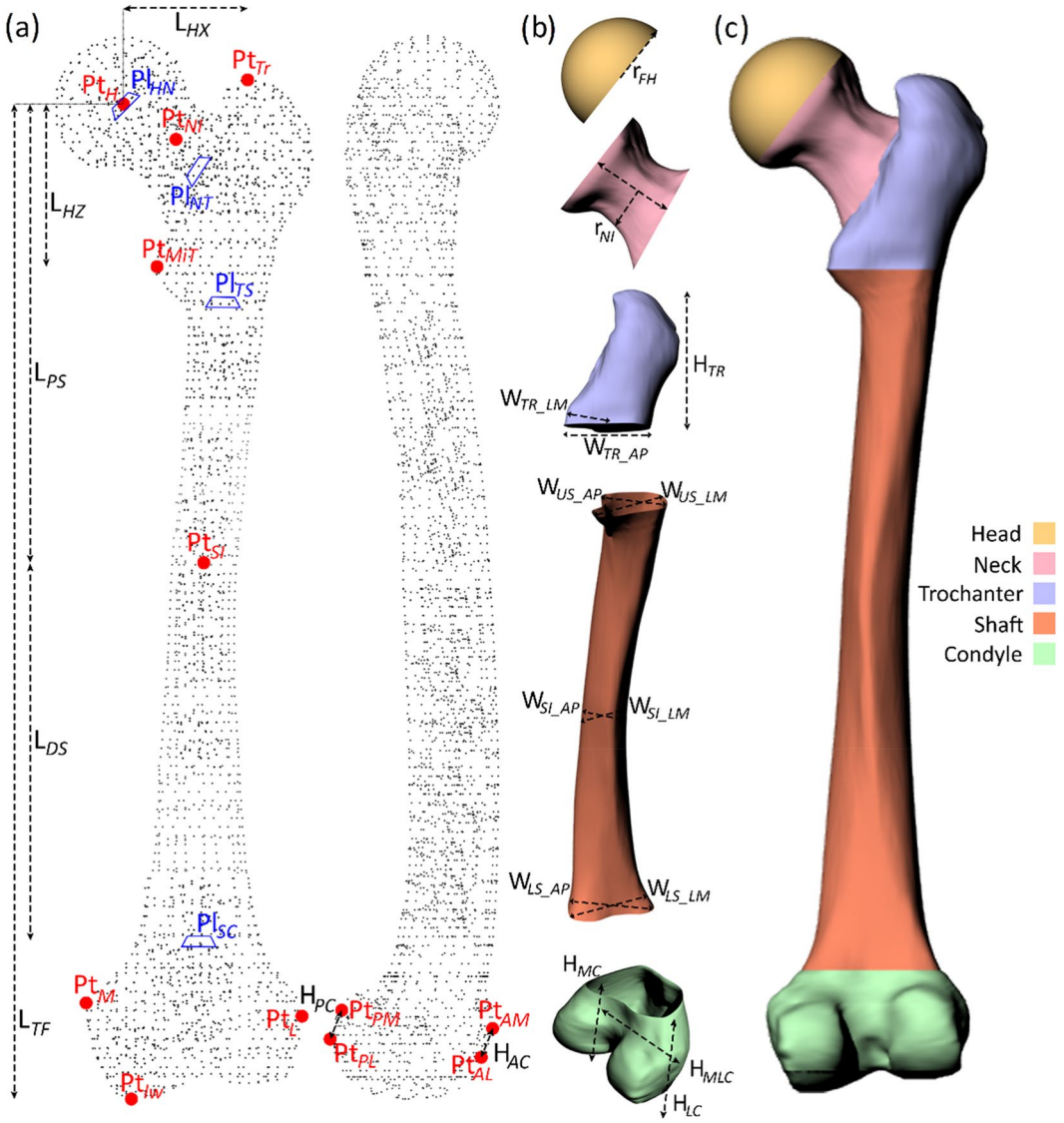

Fig. 2 **a**, **b** Definition of RGEs, feature parameters and model parameters, and **c** femur regions. RGEs: referential geometrical entities

femur model. To achieve this, a new set of parameters, called model parameters (MPs; e.g., L_{HZ}, L_{TF}), is defined (Table 2) [22], which, like the FPs, could also be extracted from 2D medical images (Figs. 2a and 2b).

We assumed that the defect area is in the shaft region, which starts at 20 mm below the minor trochanter (Pt_{MiT}) and ends at 20 mm above where the condyle part begins (Pl_{SC}). The FPs and MPs are selected to ensure that the representation of the shaft region will be as accurate as possible and that the subsequent customized scaffold will have the best fit.

The FPs and MPs are measured using the 2D medical images of a patient. These measurements are then used as input to construct the anatomical and referential coordinate systems of the new femur model. The cross-sections, obtained from the initial femur model, are proportionated with respect to those parameters. Using the newly constructed coordinate systems, the proportionated cross-sections are placed properly with the necessary transformation matrices. With lofting and filling, the freeform surface of the new femur is constructed.

Modular scaffold block creation

To create the modular blocks, a computational geometry-based algorithm, Algorithm II, was previously developed [27]. Algorithm II uses the bone model as input and performs a computational geometry-based process to create the modular blocks. The bone model can be representative of a particular group or a patient and is created using a femur

Table 1 The definition of referential geometrical entities (RGEs)

RGE	Definition
Pt_H	Femoral head center
Pt_{NI}	Femoral neck isthmus
Pt_{Tr}	The highest point of major trochanter
Pt_{MiT}	The most prominent point of minor trochanter on medial side
Pt_{SI}	Femoral shaft isthmus—origin
Pt_M	The most prominent point of condyle on medial side
Pt_L	The most prominent point of condyle on lateral side
Pt_{lw}	The lowest point of femur
Pt_{AM}	The most prominent point of condyle on AM
Pt_{PM}	The most prominent point of condyle on PM
Pt_{PL}	The most prominent point of condyle on PL
Pt_{AL}	The most prominent point of condyle on AL
Pl_{HN}	Interface plane between head and neck
Pl_{NT}	Interface plane between neck and trochanter
Pl_{TS}	Interface plane between trochanter and shaft
Pl_{SC}	Interface plane between shaft and condyle

AM: anteromedial side; PM: posteromedial side; PL: posterolateral side; AL: anterolateral side

Table 2 The definition of feature parameters (FPs) and model parameters (MPs)

FPs and MPs	Definition
r_{FH}	Femoral head radius
L_{HX}	Head offset along *X*-axis
L_{HZ}	Head offset from Pt_{MiT} along *Z*-axis
r_{NI}	Neck isthmus radius
L_N	Neck length
α_N	Neck angle
H_{TR}	Trochanter height
W_{TR_AP}	Trochanter width on AP
W_{TR_LM}	Trochanter width on LM
W_{US_AP}	Upper shaft width on AP
W_{US_LM}	Upper shaft width on LM
W_{SI_AP}	Shaft isthmus width on AP
W_{SI_LM}	Shaft isthmus width on LM
W_{LS_AP}	Lower shaft width on AP
W_{LS_LM}	Lower shaft width on LM
L_{PS}	Proximal shaft length
L_{DS}	Distal shaft length
L_{TF}	Total length of femur
α_B	Bow angle in L–M plane
H_{LC}	Lateral condylar height
H_{MC}	Medial condylar height
L_{MLC}	Medial–lateral condylar length
L_{AC}	Anterior condylar length
L_{PC}	Posterior condylar length

AP: anterior posterior plane; LM: lateral medial plane

surface-modeling algorithm or a reverse-engineering technique. This algorithm also uses mathematical inputs such as the desired height of the module, the allowable dimensional differences between the modules, and the femoral nail diameter to stack up the modules during implantation. After the average femur model and the adequate parameters are provided to Algorithm II, the algorithm creates the modular blocks specific to that group. The intramedullary nail provides not only the mechanical stability of the scaffold but also guidance for the assembly.

The shaft region of the femur is considered as the region between Pt_{MiT} and Pl_{SC}. The minimum distance between these two geometric entities on the given femur model is calculated. Using the desired module height input, the number of modules is calculated, and based on this number, the real module height is calculated. By using this height value, auxiliary planes are created through the shaft region of the femur (Fig. 3a). At the created auxiliary planes, the femur surface is sliced to obtain cross-sectional curves (Fig. 3b). With the provided inputs, the most similar and the least number of modules possible are created and similar cross-sectional curves are clustered (Fig. 3c). To represent the curves in a cluster with the same contour, a fitted curve is created per group (Fig. 3d). By using two neighboring fitted curves, the shape of the module is created by lofting and extrusion operations. To open the cavity for the placement of intramedullary femoral nail, Boolean operations are performed on the modules (Fig. 3e).

Continuous path planning for AM of modules

Algorithm III was previously developed to generate a toolpath planning for continuous extrusion AM [27]. This algorithm enables the manufacturing of a porous inner structure with the desired mechanical and biological properties with a continuous motion. Moreover, because of novel strut placements, the inner morphology of the femur can be mimicked.

The algorithm takes several AM process parameters as inputs: the nozzle diameter, the overlapping rate between layers, and the desired number of divisions in two consecutive layers. Geometrical inputs are also required, which are the 3D models of the modules to be printed. Consequently, the algorithm generates zigzag and spiral patterns in odd- and even-numbered layers, respectively. Furthermore, this creates a g-code file to control the 3D printer movements. The developed 3D models can then be used for any AM process.

The first step in creating modular blocks via AM is to slice the model into layers. This slicing process uses the desired nozzle diameter and overlapping rate that determine the number of layers and layer height (Fig. 4a). The cross-sections of the 3D scaffold are then extracted at the calculated layer heights (Fig. 4b). The outer contour represents

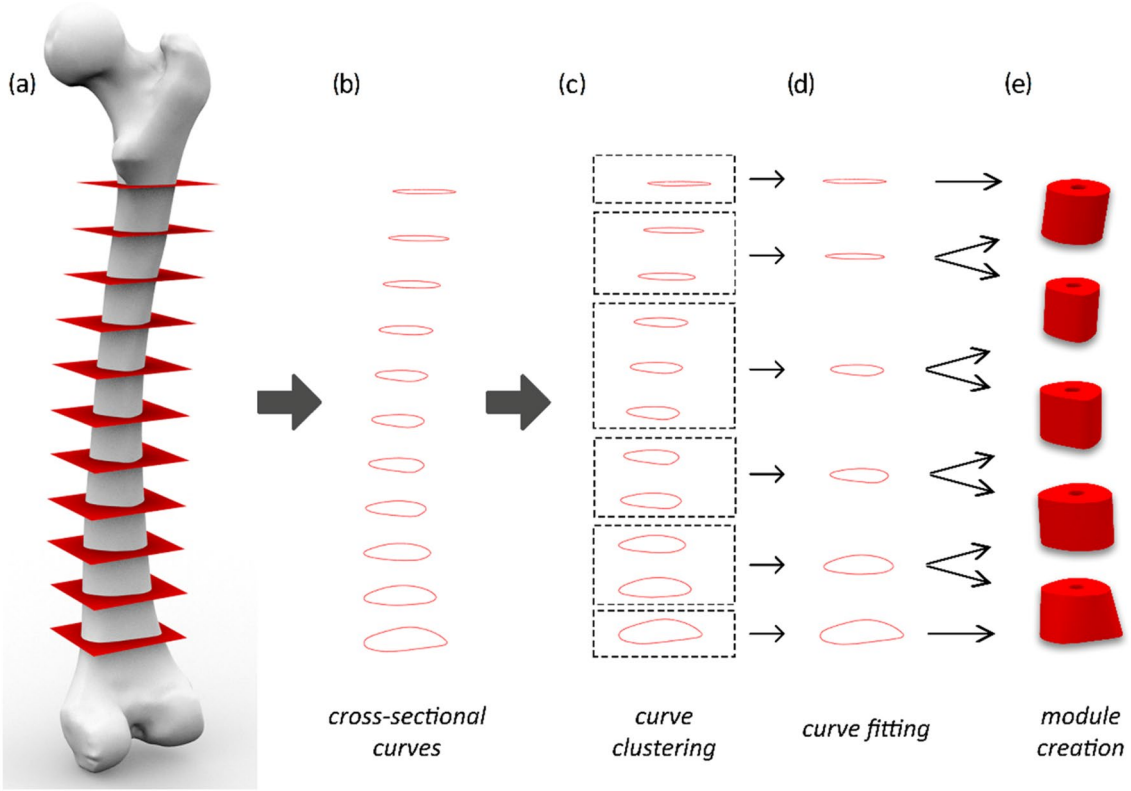

Fig. 3 The general steps for Algorithm II: **a** creation of auxiliary planes, **b** obtaining the cross-sectional curves, **c** clustering the cross-sectional curves, **d** curve fitting, and **e** 3D model of modules

the surface of the femur, and the inner circle represents the cross-section of an intramedullary nail.

In the first layer i, radial auxiliary lines are a user-specified parameter and are created using the center of the inner circle as a reference point (Fig. 4c). The intersection points in this layer are obtained by using the created auxiliary lines and the extracted cross-sectional curves (Fig. 4d). These points are stored in a local matrix, allowing the extrusion-based 3D printer to move in a zigzag pattern at that layer (Fig. 4g); the zigzag pattern starts and ends at the intersection point on the outer contour. In the next layer ($i+1$), auxiliary lines are generated using the projection of the intersection points from the previous layer i onto this layer (Fig. 4e). The auxiliary lines are equally divided using another user-specified parameter, and the intersection points are obtained (Fig. 4f). The coordinate information of these points is stored in another local matrix and a spiral pattern is created based on their radial distances from the center of the inner circle (Fig. 4h). The spiral pattern starts from the outer contour and ends at the inner contour, as the previous zigzag pattern ends at the outer contour. In the third layer ($i+2$), the zigzag pattern is created using the same process as in the first layer i, but the start point is the cross-section point at the inner circle (Fig. 4i). In the fourth layer ($i+3$), the spiral pattern is created using the same rules as in the second layer ($i+1$), but the points were stored so the spiral pattern starts from the intersection point at the inner circle (Fig. 4j). The endpoint of this pattern is at the outer contour. This four-step process is repeated until the entire scaffold module is generated. The algorithm prevents self-intersections between the connecting line segments and contours while generating the patterns. Finally, the local matrices from each layer are merged into a global matrix, which is used to generate instructions for the custom extrusion printer to follow. These instructions represent the path that the printer should take and are the output of the algorithm.

Customized scaffold structure

Algorithm IV (Fig. 5) was generated to inform a clinician in the field about how a customized best-fitting scaffold can be created using the already printed bone bricks, M_k, where k represents the total number of different modules. By using the same 2D medical images to obtain the femur model of a patient (V_{patient}), a bone defect area can be introduced to the algorithm. Two pieces of information, D_{z1} and D_{z2}, are required by the algorithm to detect the defect area, which are the linear distances of the most

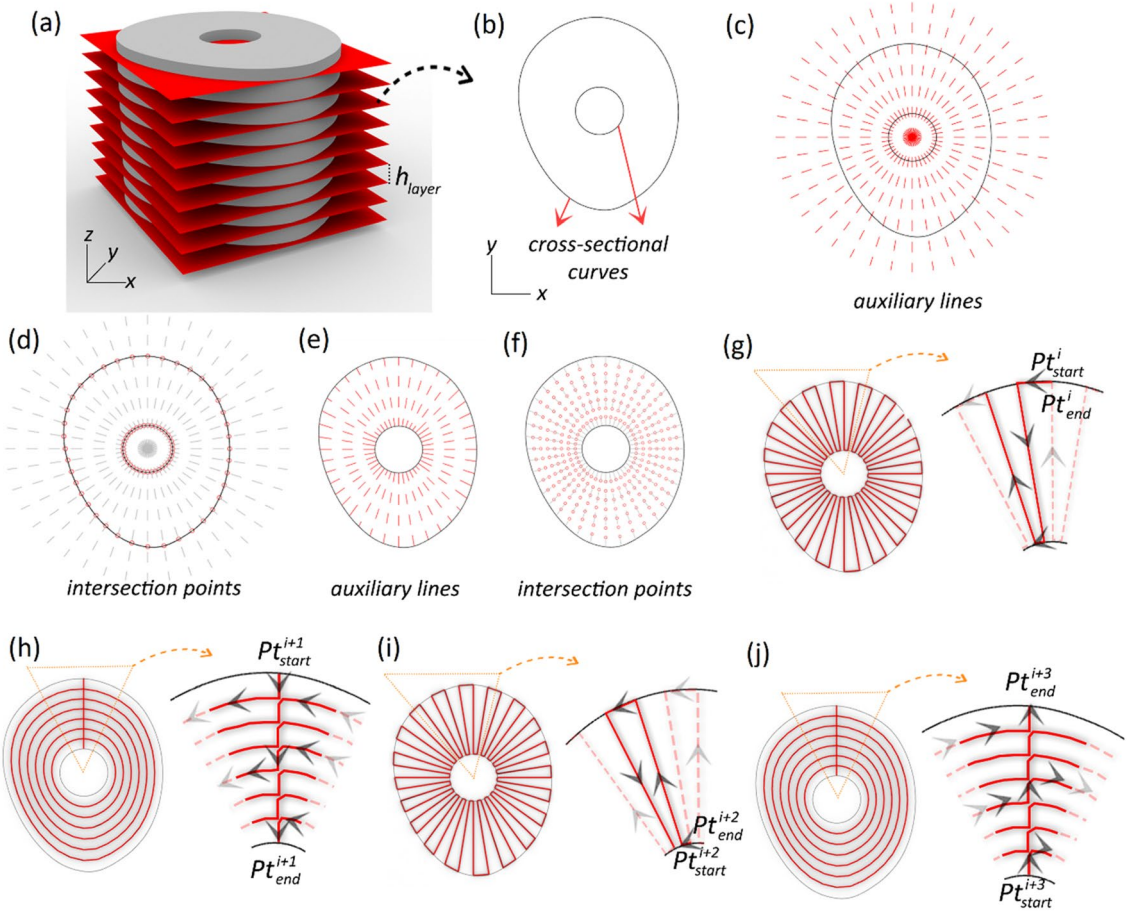

Fig. 4 The general steps for Algorithm III: **a** slicing, **b** extracting the cross-sectional curves, **c** auxiliary lines created at *i*th and $(i+2)$th layers, **d** intersection points between auxiliary lines and cross-sectional curves at *i*th and $(i+2)$th layers, **e** auxiliary lines created at $(i+1)$th and $(i+3)$th layers, **f** intersection points between auxiliary lines and cross-sectional curves at $(i+1)$th and $(i+3)$th layers, **g** the creation of a zigzag pattern at the *i*th layer, **h** the creation of a spiral pattern at the $(i+1)$th layer, **i** the creation of a zigzag pattern at the $(i+2)$th layer, and **j** the creation of a spiral pattern at the $(i+3)$th layer

prominent points of the defect along the world-*Z*-axis from Pt_{MiT}. By using this information and the height of the printed modules (h_{module}), the algorithm calculates the final top and bottom planes of the defect (Pl_t and Pl_b). These planes are used by the surgeon to perform cutting operations on the native bone tissue to prepare it for implantation. These planes are also used to create cross-sectional curves in the defect area of the patient: $CO_q, q = 0, 1, \ldots, Q$, where q represents the total number of cross-sectional curves along the defect area. Each obtained curve is divided such that the distances between the created points are equal. These points are represented by $Pt_{CO^q_{DN}}$, where DN represents the total number of points at each curve. To match the defect area with the created blocks, the obtained cross-sections are compared with those of the modules (C_k). The curves that are in the allowable range ($D_{allowable}$) are moved to the correct places using the appropriate transformation matrices. Thus, the best-fitting customized scaffold is created. From this step, the algorithm also extracts and generates information about how to assemble the modules that are going to be used and in what order. This instructional output (B_q) helps the surgeon create the scaffold structure by stacking the specified modules with the help of the intramedullary femoral nail and implant the final structure into the body.

Results and discussion

The CT scans of four different femur models, Femurs A–D, were imported into Mimics version 14.1 (Materialise, Leuven, Belgium) for editing and their 3D reconstruction. The same femur models were also created with the generated femur surface modeling algorithm by extracting the necessary measurements from 2D medical images (Fig. 6).

INPUT: V_{patient}, D_{z1}, D_{z2}, $D_{\text{allowable}}$, M_k
OUTPUT: B, Pl_t, Pl_b
START

```
1.  Create_Patient_Specific_Scaffold() {
2.  CO_q ← {} ; B_q ← {}            /*Initialization*/
3.  Pl_t & Pl_b ← Calculate(D_Z1, D_Z2, h_module)   /*Calculation of the defect area that will be represented with modules*/
4.  CO_q ← CrossSection(V_defect, Pl_t, Pl_b, h_module)  /*Cross sections of the bone defect area of the patient*/
5.  While ( i < q ) {
6.  j ← 0
7.   While (j < k) {
8.    m ← 0
9.    While ( m < DN) {
10.     Pt_i ← ClosestPoint(Pt_CO_m^i , C_j )
11.     D = Distance(Pt_i , Pt_CO_m^i )
12.     If (D ≤ D_allowable) {
13.      If ( m = DN − 1) {
14.         V_i ← VectorCreate(Pt_Center_Ci , Pt_Center_COj ) /*Moving the proper module to the right place*/
15.         B_i ← CopyObject(M_j , V_i)      /*Replacing the defect area with proper modules*/
16.         m = DN; j = k
17.       Else
18.         m = m + 1       } /*End of If Statement*/
19.     Else
20.       If ( j = k − 1) {
21.         j = k
22.       Else
23.         m = DN      } /*End of If Statement*/
24.                   }                 /*End of If Statement */
25.                 }              /*End of 3rd While Statement*/
26.              }                 /*End of 2nd While Statement*/
27. i = i + 1
28.              }                 /*End of 1st While Statement*/
29. } END                        /*End of Create_Patient_Specific_Scaffold*/
```

END

Fig. 5 Pseudocode for Algorithm IV: creation of a customized scaffold with bone bricks

To demonstrate the accuracy of the model generated by the developed algorithm, the absolute average maximum distance of the models, created with both methods, was calculated. Therefore, since the best-fitting scaffolds are produced for the shaft region, representing the femur surface in that region as closely as possible to the original one is crucial. The average distance in this region of the four different femur models was calculated as (1.2485±0.2915) mm. Considering that the best-fitting scaffolds are quickly produced, this is an acceptable average distance in this region [28, 29]. The surgeon determines the required accuracy for the case and selects the appropriate scaffold blocks from a palette of modules to create a best-fitting scaffold for the patient.

As shown in Fig. 6, Femurs A, B, and C exhibit similar morphological features. The morphological features of Femur B represent the average femur model of these three femur models (A–C). Thus, Femur B was used as a geometry-based input during the module creation process.

As described earlier, the module creation algorithm requires several user inputs, such as the height of the module and tolerance, in addition to the geometry-based input. Table 3 shows the effect of these mathematical inputs on the modules and the representation of the femur, and Fig. 7 displays the different palettes of modules created for the

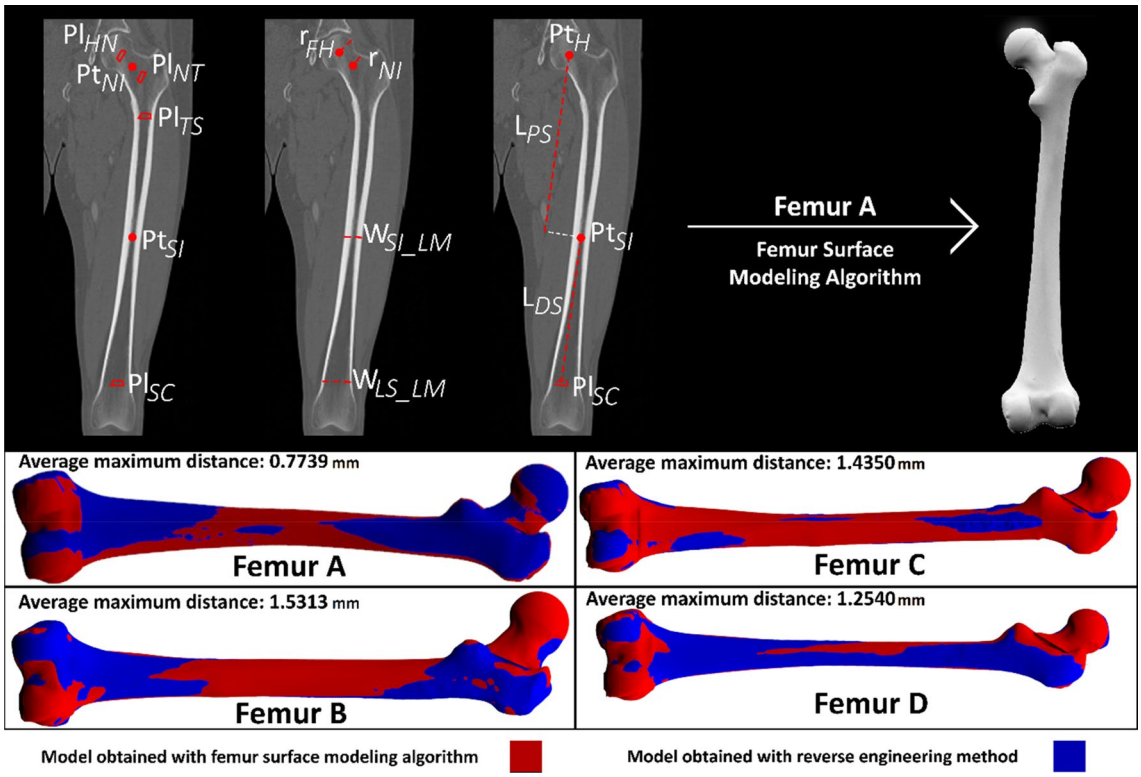

Fig. 6 Different femur models obtained with the reverse engineering method (blue) and femur surface modeling algorithm (red)

Table 3 Effects of mathematical inputs on the module creation algorithm

	Tolerance (mm)	Desired module height (mm)	Actual module height (mm)	Total number of different modules
Palette 1	0.50	5.00	5.20	25
Palette 2	1.00	5.00	5.20	14
Palette 3	2.00	5.00	5.20	7
Palette 4	0.50	10.00	10.02	19
Palette 5	1.00	10.00	10.02	12
Palette 6	2.00	10.00	10.02	7
Palette 7	0.50	15.00	15.63	15
Palette 8	1.00	15.00	15.63	10
Palette 9	2.00	15.00	15.63	5

entire shaft region of Femur B. To ensure that the entire shaft region (with a specific length) of an average femur is represented with modules without any leftover areas, the actual module height is calculated using the desired module height input and the calculated number of modules in relation to this input.

In the defined region, the topological features of cross-sectional curves in the upper part are relatively similar to each other because of the morphological characteristics of the femur. Consequently, the number of different modules required to represent this part of the region is less than that required for the distal part of the shaft region. Hence, most of the variations in the modules occur in the lower part. Therefore, even if the tolerance input decreases, the total number of distinct modules does not significantly change despite the module height input. Although the module height input provided to the system may not have a noticeable effect, the quality of the fit of the created scaffold structure on the patient is largely influenced by the module height. Additionally, the module height must provide sufficient dimensional flexibility for a surgeon to manipulate during assembly and implantation.

To illustrate the effect of these parameters on modules and the final scaffold structure, patient-specific scaffolds

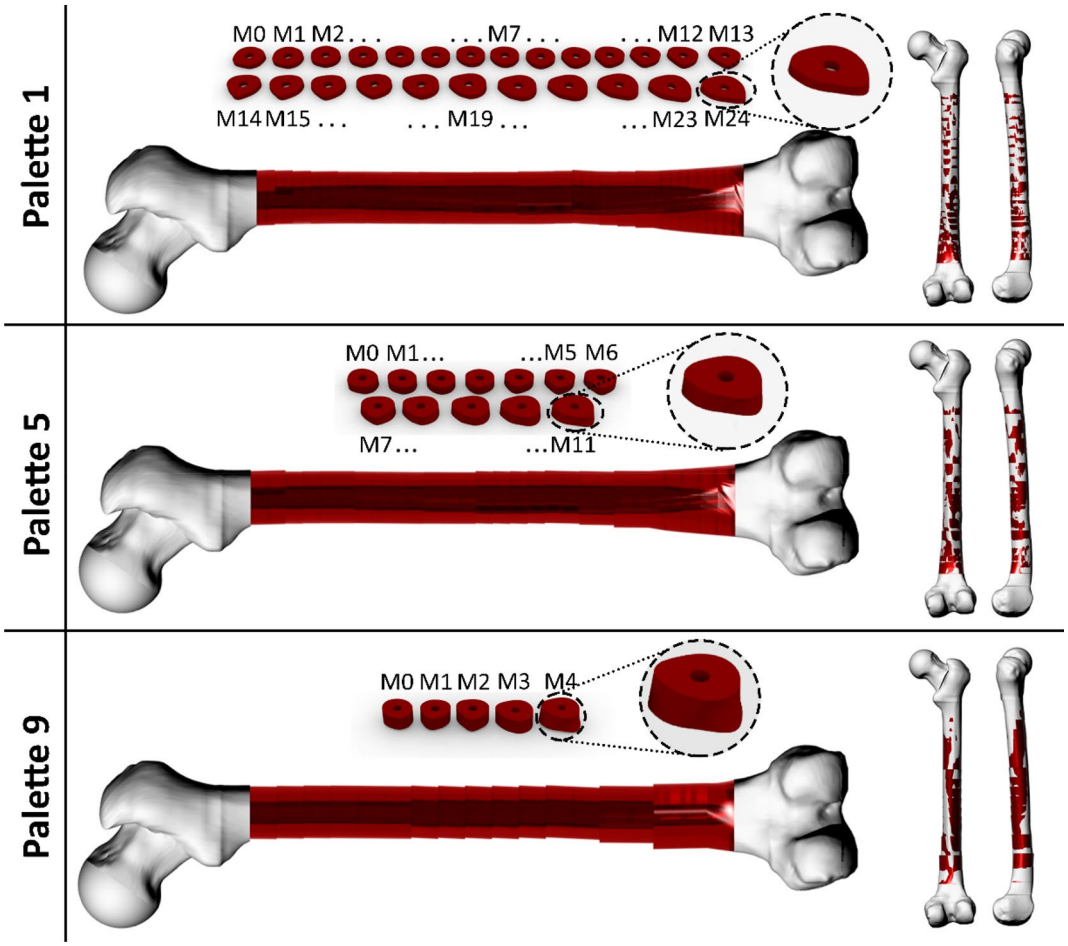

Fig. 7 Different palettes of scaffold blocks

were created with different bone brick palettes for different cases (Fig. 8). The first scenario was where a large bone defect was observed around the distal part of the shaft region of Femur C. The defect height (the length along the sagittal/coronal plane, *Z*-axis) was 67.60 mm. The information on where the defect was located was introduced to the system. The modules belonging to Palettes 1, 4, and 7, created from Femur B, were uploaded to the system as defaults, respectively. Consequently, the system gave the best-fitting scaffold to the scenario for Femur C (Figs. 8a, 8c and 8e). Moreover, information for the assembly of the proper modules was extracted. The same procedure was followed for Femur A with a defect having similar specifications (Figs. 8b, 8d and 8f). For another scenario, a large bone defect around the middle shaft region was examined for both Femurs A and C. The height of this defect was 109.20 mm. After the femur models were generated, the defect area was introduced to the system. Correspondingly, the best-fitting scaffold and assembly information, created with the defined default module palettes, were obtained for both Femurs A and C (Figs. 8a, 8b and 8f).

The resulting scaffold structures created with Palette 1 have smoother surfaces than those created with Palettes 4 and 7. When the values of the tolerance and height inputs of Algorithm IV decrease, the representation of the patient femur increases in accuracy. Additionally, obtaining a better-fitting scaffold structure becomes possible. Nonetheless, one limitation regarding using Palette 1 is that the total number of different modules is higher. Therefore, a surgeon may find it difficult to create the best-fitting scaffold for a patient with a large bone defect when dealing with such small structures.

When implanting the created scaffold into the body, the height of the created structure becomes as important as its accurate surface representation. The clinician must clean the defect bone area from excess tissue to enable the scaffold structure to fit the defect area properly. Performing minimum changes without losing too much native tissue is directly related to the height difference between the final scaffold structure and defect area. The scaffold structure, created with modules belonging to Palette 7 for a 67.60-mm sized defect (Figs. 8c and 8d), is the structure where the most changes must be made because of the height difference between the

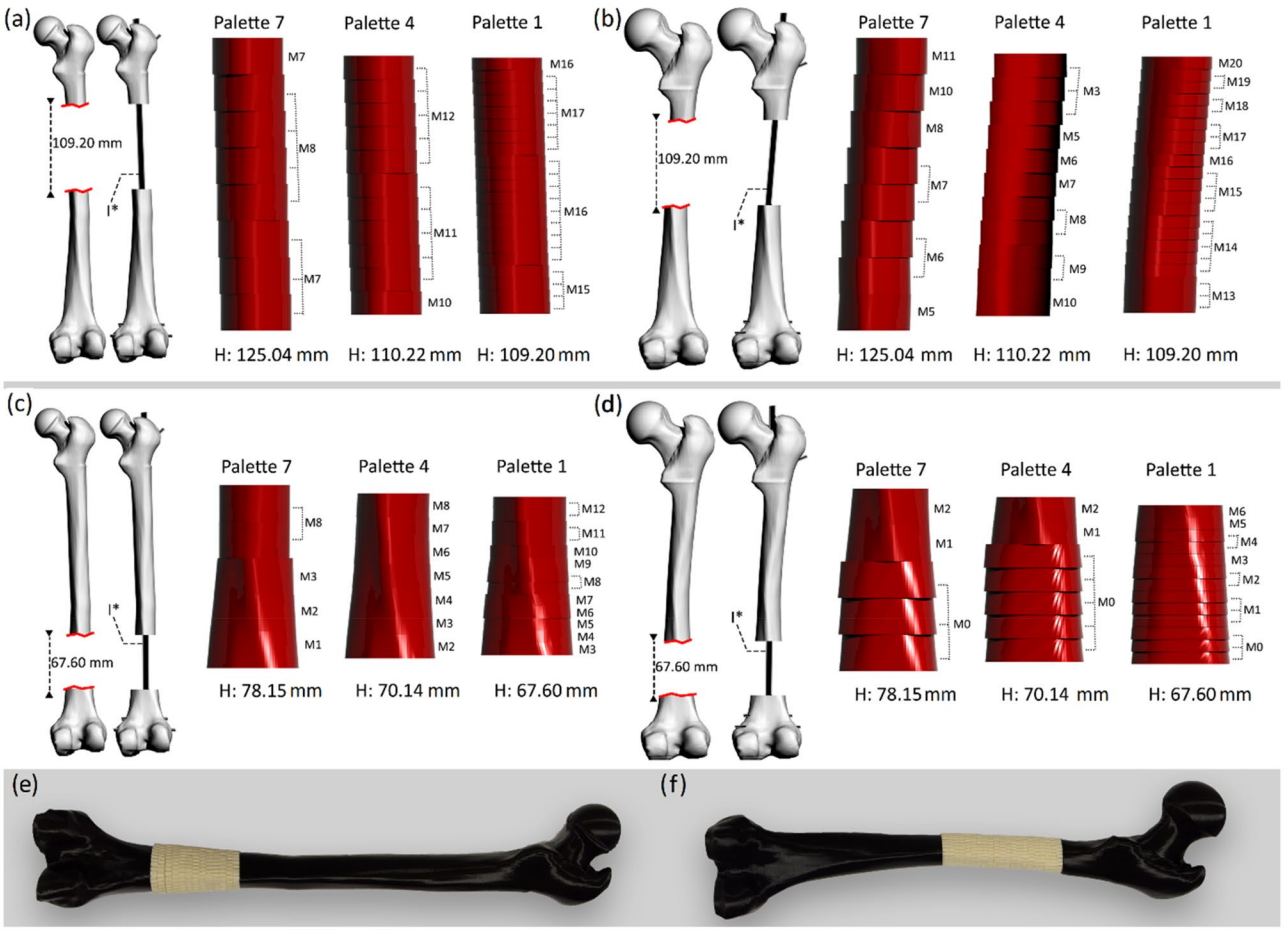

Fig. 8 Best-fitting scaffolds for femur model C (**a**, **c**, and **e**) and A (**b**, **d**, and **f**) with 67.60-mm distal (**c**, **d**, and **e**) and 109.20-mm shaft (**a**, **b**, and **f**) defects with different palettes of bone bricks (Palettes 1, 4, and 7). Printed prototypes of femur model C with 67.60-mm distal (**e**) and femur model A with 109.20-mm shaft defects (**f**)

defect and the scaffold, which was 10.55 mm. This was followed by the scaffold created with Palette 4 modules, which had a height difference of 2.54 mm.

However, this was not the same for scaffolds produced for femur models with a 109.20-mm sized shaft defect (Figs. 8a and 8b). Here, the amount of removal of native tissue is greater when the scaffold structure is created with modules belonging to Palette 4 rather than Palette 7 (1.02 and 0.21 mm, respectively). Although the maximum amount of native tissue that needs to be removed has a direct relationship with the module height, this is also affected by the defect height. Therefore, whichever group is targeted, the most common defect in that group can be analyzed by performing a statistical study of the location of the defect and the most common defect height to decide the height of the modules.

Prototypes of different scaffold structures and femur models were manufactured with commercially available 3D printers and software (Figs. 8e and 8f). Additionally, to produce scaffolds with the generated novel zigzag/spiral pattern, Algorithm III was implemented with scripting tools of Rhinoceros 3D (RhinoScript and Python for Grasshopper) running on a PC to obtain the instruction file to control the custom extrusion-based 3D printer. The 3D printer has a heated syringe where polycaprolactone (PCL; 37 kDa molecular weight) was melted at 65 °C. With a pneumatic dispensing unit, melted PCL was extruded through a 250-μm diameter nozzle until the whole modular block was manufactured layer by layer. All the modular blocks used to create the scaffold structure for the 67.60-mm distal bone defect were printed as shown in Figs. 8e and 9a. Figure 9 displays some of them, i.e., Modules M3 (Fig. 9g), M6 (Fig. 9f), M9 (Fig. 9e), and M12 (Fig. 9b), and the different porosity levels of M12 (Figs. 9c and 9d). The developed algorithms can generate modular scaffolds in several hours on a high-end PC.

When the same first and second division numbers are used as inputs in Algorithm III to produce each module, the location of the pore in each module will be almost the same. Thus, if an obtained scaffold structure created with such

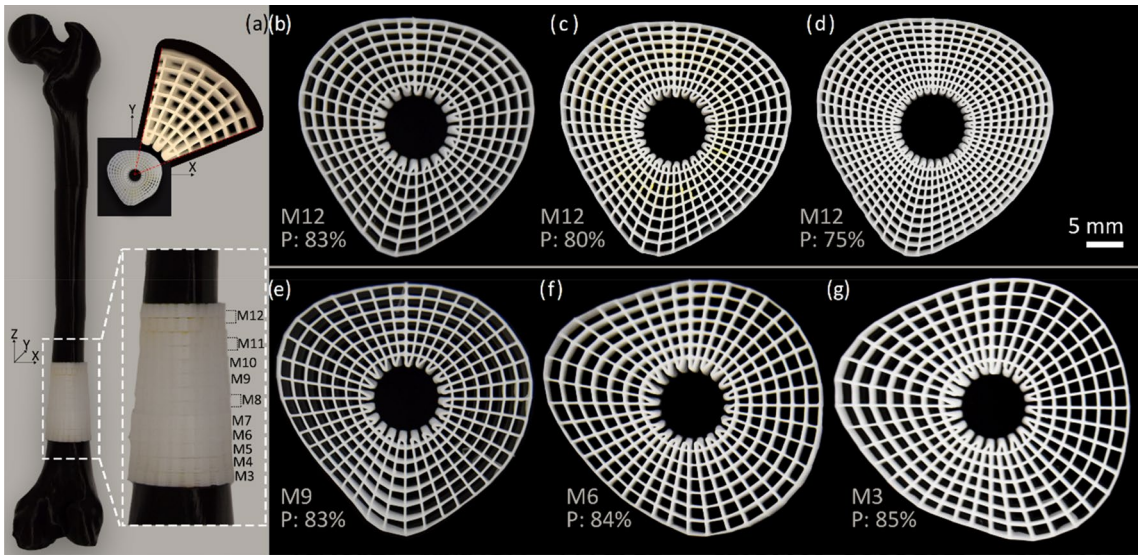

Fig. 9 **a** Assembly of the best-fitting scaffold with modules of Palette 1. **b**, **e**–**g** Top views of the created structure for M12 (**b**), M9 (**e**), M6 (**f**), and M3 (**g**) created with the same inputs of Algorithm III. **c**, **d** The resultant M12 scaffold blocks with different parameters of Algorithm III. P: porosity

printed modules is viewed from above, the pores extending all the way through the structure can be seen (Fig. 9a). Using the same parameters also causes the total porosity of the modules to be similar to each other (Figs. 9b and 9e–9g).

Conclusions and future directions

Herein, a novel approach was proposed to create the customized scaffolds of best fit for large bone defects using modular, bioactive, low-cost, and 3D-printed bone scaffold blocks. A femur surface-modeling algorithm was developed to generate 3D patient-specific femur scaffolds for the patient, eliminating the need for time-consuming and expensive steps such as 3D reconstruction from 2D medical images. The scaffold block creation algorithm was developed to parametrically obtain scaffold modules with desired topological characteristics to best represent the defect area. To mimic the bone morphology and obtain an adequate porous structure, a computational algorithm was generated to create a continuous zigzag/spiral tool path for modules. With a custom extrusion-based 3D printer, the porous bone bricks were additively manufactured with a biodegradable polymer. The final algorithm was designed to inform the clinician about the number and type of on-demand modules needed to create a best-fitting, patient-specific scaffold to represent the bone defect area. This study presents a promising solution for creating a custom-fitted scaffold for large bone defects directly from 2D medical images of a patient with reduced time, cost, and effort. For ongoing development, these algorithms can be implemented into software with a user-friendly and interactive interface for surgeons. The methods developed here can create modular and customizable scaffold blocks that can be adapted to fit the bone defect area of a patient. These customized scaffold blocks are obtained directly from 2D images and can be 3D printed to be used for femoral bone defects. However, the developed methods need to be modified and generalized for other types of defect areas. More specifically, the parameters required to model the bone tissue need to be defined. The developed scaffolds are fabricated from biodegradable polymeric materials to support and guide cells to form their own extracellular matrix. For critical bone defects, scaffolds should be combined with active biomolecules to allow nutrient and metabolite exchange, and thus to retain cellular activity [30]. However, the in vitro and in vivo studies leading to clinical applications are beyond the scope of this study.

Acknowledgements This research is supported by the Engineering and Physical Sciences Research Council (EPSRC) of the UK, the Global Challenges Research Fund (GCRF), Grant Number EP/R015139/1. This paper presents original research work that was conducted as part of a master's thesis at Sabanci University [20]. The authors would like to thank Sabanci University and Nanotechnology Research and Application Center.

Author contributions AAA: methodology, software, investigation, writing—original draft, and visualization; BK: supervision, writing—review and editing, conceptualization, and funding acquisition; ED: conceptualization; AW, GC, GB, and PB: conceptualization and funding acquisition.

Declarations

Conflict of interest PB is an editorial board member for *Bio-Design and Manufacturing* and was not involved in the editorial review or the decision to publish this article. The authors declare that they have no conflict of interest.

Ethical approval This article does not contain any studies with human or animal subjects performed by any of the authors.

References

1. Schemitsch EH (2017) Size matters: defining critical in bone defect size! J Orthop Trauma 31:S20–S22. https://doi.org/10.1097/BOT.0000000000000978
2. Arrington ED, Smith WJ, Chambers HG et al (1996) Complications of iliac crest bone graft harvesting. Clin Orthop Relat Res 329:300–309. https://doi.org/10.1097/00003086-199608000-00037
3. Banwart JC, Asher MA, Hassanein RS (1995) Iliac crest bone graft harvest donor site morbidity: a statistical evaluation. Spine 20(9):1055–1066. https://doi.org/10.1097/00007632-199505000-00012
4. Flierl MA, Smith WR, Mauffrey C et al (2013) Outcomes and complication rates of different bone grafting modalities in long bone fracture nonunions: a retrospective cohort study in 182 patients. J Orthop Surg Res 8(1):33. https://doi.org/10.1186/1749-799X-8-33
5. Polo-Corrales L, Latorre-Esteves M, Ramirez-Vick JE et al (2014) Scaffold design for bone regeneration. J Nanosci Nanotechnol 14(1):15–56. https://doi.org/10.1166/jnn.2014.9127
6. Kim T, See CW, Li XC et al (2020) Orthopedic implants and devices for bone fractures and defects: past, present and perspective. Eng Regen 1:6–18. https://doi.org/10.1016/j.engreg.2020.05.003
7. Ji CD, Annabi N, Hosseinkhani M et al (2012) Fabrication of poly-DL-lactide/polyethylene glycol scaffolds using the gas foaming technique. Acta Biomater 8(2):570–578. https://doi.org/10.1016/j.actbio.2011.09.028
8. Wu X, Liu Y, Li X et al (2010) Preparation of aligned porous gelatin scaffolds by unidirectional freeze-drying method. Acta Biomater 6(3):1167–1177. https://doi.org/10.1016/j.actbio.2009.08.041
9. Pirhonen E, Moimas L, Haapanen J et al (2003) Porous bioactive 3-D glass fiber scaffolds for tissue engineering applications manufactured by sintering technique. Key Eng Mater 240–242:237–240. https://doi.org/10.4028/www.scientific.net/kem.240-242.237
10. Nandakumar A, Fernandes H, De Boer J et al (2010) Fabrication of bioactive composite scaffolds by electrospinning for bone regeneration. Macromol Biosci 10(11):1365–1373. https://doi.org/10.1002/mabi.201000145
11. Garg T, Singh O, Arora S et al (2012) Scaffold: a novel carrier for cell and drug delivery. Crit Rev Ther Drug Carrier Syst 29(1):1–63. https://doi.org/10.1615/CritRevTherDrugCarrierSyst.v29.i1.10
12. Christensen AM, Passalacqua NV, Bartelink EJ (2014) Forensic Anthropology: Current Methods and Practice. Academic Press, London. https://doi.org/10.1016/C2013-0-09760-5
13. Peacock M, Buckwalter KA, Persohn S et al (2009) Race and sex differences in bone mineral density and geometry at the femur. Bone 45(2):218–225. https://doi.org/10.1016/j.bone.2009.04.236
14. Rawal BR, Ribeiro R, Malhotra R et al (2012) Anthropometric measurements to design best-fit femoral stem for the Indian population. Indian J Orthop 46(1):46–53. https://doi.org/10.4103/0019-5413.91634
15. Mahaisavariya B, Sitthiseripratip K, Tongdee T et al (2002) Morphological study of the proximal femur: a new method of geometrical assessment using 3-dimensional reverse engineering. Med Eng Phys 24(9):617–622. https://doi.org/10.1016/S1350-4533(02)00113-3
16. Turnbull G, Clarke J, Picard F et al (2018) 3D bioactive composite scaffolds for bone tissue engineering. Bioact Mater 3(3):278–314. https://doi.org/10.1016/j.bioactmat.2017.10.001
17. Zhang L, Yang GJ, Johnson BN et al (2019) Three-dimensional (3D) printed scaffold and material selection for bone repair. Acta Biomater 84:16–33. https://doi.org/10.1016/j.actbio.2018.11.039
18. Zadpoor AA (2020) Meta-biomaterials. Biomater Sci 8(1):18–38. https://doi.org/10.1039/c9bm01247h
19. McCall TA, Brokaw DS, Jelen BA et al (2010) Treatment of large segmental bone defects with reamer-irrigator-aspirator bone graft: technique and case series. Orthop Clin North Am 41(1):63–73. https://doi.org/10.1016/j.ocl.2009.08.002
20. Acar AA (2020) Designing and additive manufacturing of customizable, modular scaffold blocks for large bone defects. MS Thesis, Sabanci University, Istanbul, Türkiye
21. Stojkovic M, Milovanovic J, Vitkovic N et al (2012) Analysis of femoral trochanters morphology based on geometrical model. J Sci Ind Res 71(3):210–216
22. Chen XZ, He KJ, Chen ZM et al (2015) Quick construction of femoral model using surface feature parameterization. MCB Mol Cell Biomech 12(2):123–146. https://doi.org/10.3970/mcb.2015.012.123
23. McNeel R (2020) Grasshopper-generative modelling with Rhino. McNeel North America, Seattle, USA. https://www.grasshopper3d.com. Accessed 24 Nov, 2023
24. McNeel R (2020) Rhinoceros-NURBS modeling for Windows (version 6.0). McNeel North America, Seattle, USA. https://www.rhino3d.com. Accessed 24 Nov, 2023
25. Wu G, Van Der Helm FCT, Veeger HEJ et al (2005) ISB recommendation on definitions of joint coordinate systems of various joints for the reporting of human joint motion-Part II: shoulder, elbow, wrist and hand. J Biomech 38(5):981–992. https://doi.org/10.1016/j.jbiomech.2004.05.042
26. Chantarapanich N, Rojanasthien S, Chernchujit B et al (2017) 3D CAD/reverse engineering technique for assessment of Thai morphology: proximal femur and acetabulum. J Orthop Sci 22(4):703–709. https://doi.org/10.1016/j.jos.2017.02.003
27. Koc B, Acar AA, Weightman A et al (2019) Biomanufacturing of customized modular scaffolds for critical bone defects. CIRP Ann 68(1):209–212. https://doi.org/10.1016/j.cirp.2019.04.106
28. Chen XZ, He KJ, Chen ZM et al (2016) A parametric approach to construct femur models and their fixation plates. Biotechnol Biotechnol Equip 30(3):529–537. https://doi.org/10.1080/13102818.2016.1145555
29. Noble PC, Alexander JW, Lindahl LJ et al (1988) The anatomic basis of femoral component design. Clin Orthop Relat Res 235:148–165. https://doi.org/10.1097/00003086-198810000-00015
30. Tamaddon M, Blunn G, Tan R et al (2022) In vivo evaluation of additively manufactured multi-layered scaffold for the repair of

large osteochondral defects. Bio-des Manuf 5(3):481–496. https://doi.org/10.1007/s42242-021-00177-w

Authors and Affiliations

Anil A. Acar[1,2] · Evangelos Daskalakis[3] · Paulo Bartolo[3,4] · Andrew Weightman[3] · Glen Cooper[3] · Gordon Blunn[5] · Bahattin Koc[1,2]

✉ Bahattin Koc
bahattin.koc@sabanciuniv.edu

1 Faculty of Engineering and Natural Sciences, Sabanci University, Istanbul 34956, Türkiye

2 3D Bioprinting Laboratory, Sabanci University Nanotechnology Research and Application Center, Istanbul 34956, Türkiye

3 School of Mechanical, Aerospace and Civil Engineering, Manchester Institute of Biotechnology, University of Manchester, Manchester M13 9PL, UK

4 Singapore Centre for 3D Printing, School of Mechanical and Aerospace Engineering, Nanyang Technological University, Singapore 639798, Singapore

5 School of Pharmacy and Biomedical Sciences, University of Portsmouth, Portsmouth PO1 2UP, UK